

# Separation of Distinct Photoexcitation Species in Femtosecond Transient Absorption Microscopy

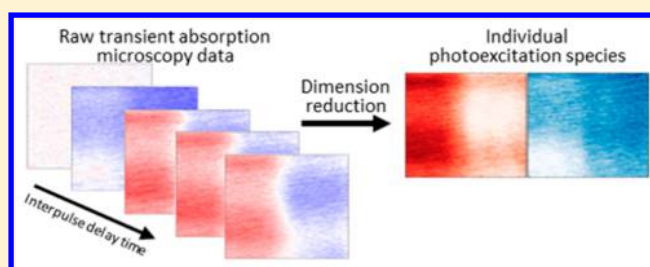
Mary Jane Simpson,<sup>†</sup> Benjamin Doughty,<sup>†</sup> Bin Yang,<sup>‡</sup> Kai Xiao,<sup>‡</sup> and Ying-Zhong Ma<sup>\*,†</sup>

<sup>†</sup>Chemical Sciences Division and <sup>‡</sup>Center for Nanophase Materials Sciences, Oak Ridge National Laboratory, Oak Ridge, Tennessee 37831, United States

## Supporting Information

**ABSTRACT:** Femtosecond transient absorption microscopy is a novel chemical imaging capability with simultaneous high spatial and temporal resolution. Although several powerful data analysis approaches have been developed and successfully applied to separate distinct chemical species in such images, the application of such analysis to distinguish different photoexcited species is rare. In this paper, we demonstrate a combined approach based on phasor and linear decomposition analysis on a microscopic level that allows us to separate the contributions of both the excitons and free charge carriers in the observed transient absorption response of a composite organometallic lead halide perovskite film. We found spatial regions where the transient absorption response was predominately a result of excitons and others where it was predominately due to charge carriers, and regions consisting of signals from both contributors. Quantitative decomposition of the transient absorption response curves further enabled us to reveal the relative contribution of each photoexcitation to the measured response at spatially resolved locations in the film.

**KEYWORDS:** perovskite, transient absorption microscopy, photoexcitation, dimension reduction, big data



Femtosecond transient absorption microscopy (TAM) is a nonlinear optical imaging technique that permits the characterization of electronic excited-state species with high spatial and temporal resolution. It also enables the mapping of excited-state processes such as photoexcitation energy flow directly within the time scale of their occurrence. The experimental data typically consist of a stack of transient absorption (TA) images acquired at various delay times between excitation (pump) and probe pulses. Each of these images represents a measure of pump-induced TA changes as a function of spatial position ( $x, y$ ) within the focal plane. Furthermore, the contributing species can exhibit variable TA signal signs, which arise from pump-induced bleaching, stimulated emission, and excited-state absorption.<sup>1</sup>

It has been shown that TAM image stacks can be readily converted into chemical images when the sample under investigation contains chemical species that have known and distinct temporal signatures.<sup>1–8</sup> However, when two or more chemical species contribute to a TAM image and their associated TA signals are spatially overlapped, unambiguous identification of the spatial distribution of each individual contributing species becomes challenging. Although selecting single or multiple delay times may discriminate species with opposite signal signs that are spatially well-separated,<sup>1–8</sup> this method may fail in common situations including (1) probing species that have the same signal sign or (2) probing species that have opposite signal signs and are overlapping spatially.

Several data analysis methods including principal component analysis (PCA),<sup>6</sup> linear decomposition,<sup>9</sup> and phasor analysis<sup>10–12</sup> have been developed and successfully applied to separate various contributing chemical species in TAM images. PCA finds the rotation of the data axes that contains the greatest variance over the entire data set. The components will be the TA response characteristics that are the most common for all of the pixels, which are not necessarily useful for identifying unique species. Phasor analysis identifies clusters of pixels with similar TA response curves. The dynamic range of the TA response curves forms the basis of a color scale, which is used to represent the corresponding pixels in the TAM image, so that pixels with similar TA responses have the same color. In linear decomposition, reference standard TA response curves are input for species of interest. These may be internal references from the TAM data set or external references from a quantitative standard. Then, amplitudes are calculated to define every TA response curve as a linear combination of the reference curves, which is solved using singular value decomposition.

While the approaches mentioned above have been successfully applied to separate different *chemical species* in TAM images, attempts to apply these methods to identify different *photoexcited species* such as neutral excitons and free charge carriers have been rare. Here, we apply phasor analysis

**Received:** November 6, 2015

**Published:** February 3, 2016

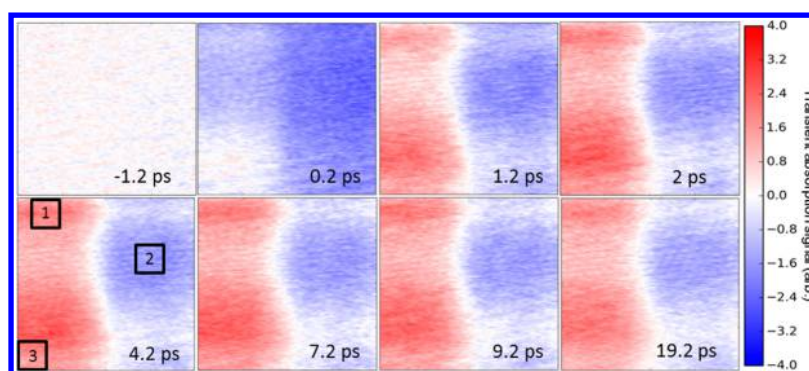


**Figure 1.** Raw TAM data at several time delays. Positive signal (red) arises from pump-induced transmission and/or stimulated emission, while negative signal (blue) represents pump-induced absorption. Images are  $20 \times 20 \mu\text{m}$  areas consisting of  $128 \times 128$  pixels. Boxes indicate regions of interest for further analysis.

and linear decomposition to distinguish the spatial distribution of neutral excitons and free charge carriers in a polycrystalline thin film of methylammonium lead tri-iodide ( $\text{CH}_3\text{NH}_3\text{PbI}_3$ ) coated with a commonly used electron acceptor, [6,6]-phenyl- $\text{C}_{61}$ -butyric acid methyl ester (PCBM), layer. Specifically, we use phasor analysis to identify spatial locations of individual species and then use linear decomposition to quantify the relative contribution of each species to the TA signal across the entire image area.

Application of these data analysis methods to separate distinct photoexcitation species such as excitons and free charge carriers in semiconducting materials that contribute simultaneously to the TAM images, to the best of our knowledge, has not been reported. The need for such an analysis can be seen, for example, for organometallic halide perovskites, which have been used in demonstrating remarkably high photovoltaic power conversion efficiency in recent years.<sup>13</sup> For these hybrid perovskites in general, and  $\text{CH}_3\text{NH}_3\text{PbI}_3$  in particular, a key fundamental question that has been debated is whether the elementary photoexcitations are either neutral excitons<sup>14–16</sup> or free charge carriers.<sup>17</sup> This arises from diverse values of the reported exciton binding energies<sup>14,16,18–24</sup> and controversial interpretations of the same experimental results.<sup>14,17</sup> Very recently, we applied femtosecond TAM to study electronic excited-state processes in several thin film systems employing  $\text{CH}_3\text{NH}_3\text{PbI}_3$  as the photoactive layer. We obtained experimental evidence for the coexistence of excitons and charge carriers under relatively high pump and probe intensities.<sup>25</sup> However, identification of these photoexcited species was attempted only for the two spatial locations with the most pronounced features and largest signal amplitudes. It remains unclear where these photoexcited species are located in space and how to quantify their relative contributions if they coexist at any given spatial location.

## RESULTS AND DISCUSSION

Figure 1 shows representative TAM images acquired for a polycrystalline  $\text{CH}_3\text{NH}_3\text{PbI}_3/\text{PCBM}$  thin film at several delay times as indicated in the figure. It can be seen from Figure 1 that these images exhibit several distinct spatial features with differing TA signal signs, i.e., either positive induced transmission or negative induced absorption. By comparing the images acquired at different delay times, one can also see that these distinct spatial features evolve over different time scales. Through detailed analysis of the TA kinetics extracted from two spatial locations with the most pronounced features and largest

signal amplitudes, we have shown recently that both free charge carriers and neutral excitons exist in this system.<sup>25</sup> This identification was realized by considering the high pump fluence used in our measurements, which will unavoidably induce nonlinear electronic excited-state processes that govern the observed dynamics. Consequently, we explicitly considered two high-intensity phenomena: exciton–exciton annihilation<sup>26</sup> and Auger recombination of charged carriers.<sup>27,28</sup> According to the analysis described in detail in refs 29 and 30, we showed that it is possible to distinguish the contributing excited-state species by simply plotting either an inverse of the normalized transient absorption signal amplitude or its square as a function of the delay time. A linear relationship between the inverse of the TA signal amplitude and delay time is expected if the contributing species are excitons, whereas for charge carriers a squared inverse of the TA signal amplitude should scale linearly with delay time instead. On the basis of this analysis, we identified that the spatial features observed at positions 2 and 3 of the TAM images shown in Figure 1 arise from free charge carriers and excitons, respectively. For all remaining regions in the image, neither the contributing species nor their relative contributions, if more than one species coexist, could be determined from our initial analysis. It is pertinent to mention that our measurements showing the coexistence of excitons and charge carriers have been substantiated by recent experimental results.<sup>31,32</sup> While a charge-trapping phenomenon reported recently,<sup>33,34</sup> especially by Ginger and co-workers using confocal fluorescence microscopy,<sup>35</sup> may lead to different TA signal signs, its occurrence would not cause the observed nonlinear relaxation behavior.

While a preliminary analysis of the TA kinetics extracted from position 1 can be reasonably reproduced by a linear combination of the kinetic traces obtained at positions 2 and 3 shown by the dashed line in Figure 2, the presence of a possible mixture of photoexcited species is not obvious from the images shown in Figure 1. In the following, we will focus on identifying the distinct contributions of charge carriers and excitons in the entire TAM images acquired at different delay times using phasor analysis and then quantifying their relative contributions with linear decomposition. An underlying assumption for the analysis of our imaging data is that excitons and free charge carriers are in thermal equilibrium, which was also invoked in the theoretical study by Stranks et al. in view of the rapid formation and dissociation of excitons.<sup>33</sup> As a result, the corresponding terms in eqs 1–3 of Stranks et al. can be neglected, and the linear superposition that our analysis invokes

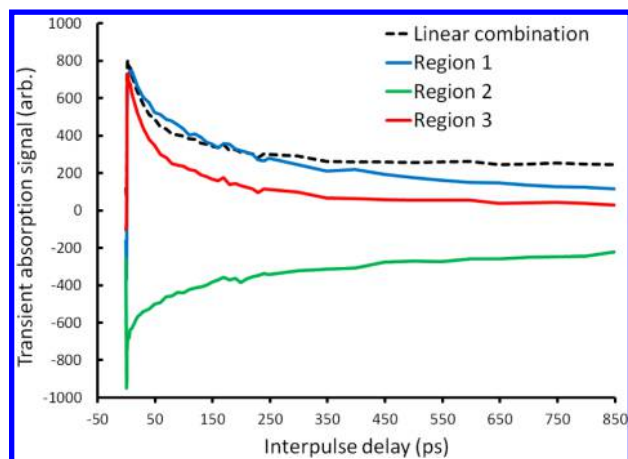


**Figure 2.** TA kinetic traces extracted from three different regions of interest, which are indicated in Figure 1. The black dashed line is obtained by linear combination of the TA kinetics obtained at positions 2 and 3, with corresponding relative contributions of 15% and 85%, respectively.

serves as a reasonable approximation to the complex dynamics taking place. It should be pointed out that in many cases linear decomposition will not be valid when the systems are either coupled or nonlinear, as is often common in analysis of transient absorption data. For the limited case here, we show in the Supporting Information that the rate constants can allow us to decouple the equations in this particular case. A detailed validation of our analysis in separating distinct species in the mixed regions of interest is given in the Supporting Information. The limited diffusion range of carriers within their lifetimes observed by Ginsberg and co-workers<sup>36</sup> and Deschler and co-workers<sup>37</sup> further suggests that exchange of photoexcitations (excitons and charge carriers) from different regions of interest can be safely neglected. This is also in line with the carrier diffusion coefficient determined by Huang and co-workers.<sup>38</sup> Using the upper limit of the reported diffusion coefficient of  $0.08 \text{ cm}^2 \text{ s}^{-1}$ , we estimate that the charge carriers can diffuse only about 160 nm within the 850 ps window probed in our measurements. A similar estimate can be made for excitons. On the basis of the reported exciton diffusion constant  $D \approx 0.01 \text{ cm}^2 \text{ s}^{-1}$ ,<sup>39</sup> we can calculate that exciton diffusion length is only 58 nm within the time delay used for our measurements (850 ps).

## ■ PHASOR ANALYSIS

Recently adapted from fluorescence lifetime imaging microscopy, phasor analysis provides a convenient way to visualize differing TA responses. Phasor analysis sorts TA responses by their signs and temporal response.<sup>10</sup> Implementing phasor analysis to analyze multidimensional TAM data sets requires calculating the normalized sine and cosine transforms for TA kinetics acquired at every pixel and then plotting those values in a 2D histogram, which is called the phasor plot.<sup>40</sup> Those pixels in a TAM data set that have similar TA response will be clustered together in the phasor plot; thereby the overall spread of the phasor plot represents the range of differing TA responses in the data set. This range of TA responses in the phasor plot histogram forms the basis of a color scale used to simplify the TAM data into a single color-coded image. The corresponding pixels in the TAM image are recolored based on their position in the phasor plot with respect to the scale bar. A

more detailed description about recoloring the TAM images based on the phasor plot is provided in the Supporting Information. Figure 3 shows the recolored image based on

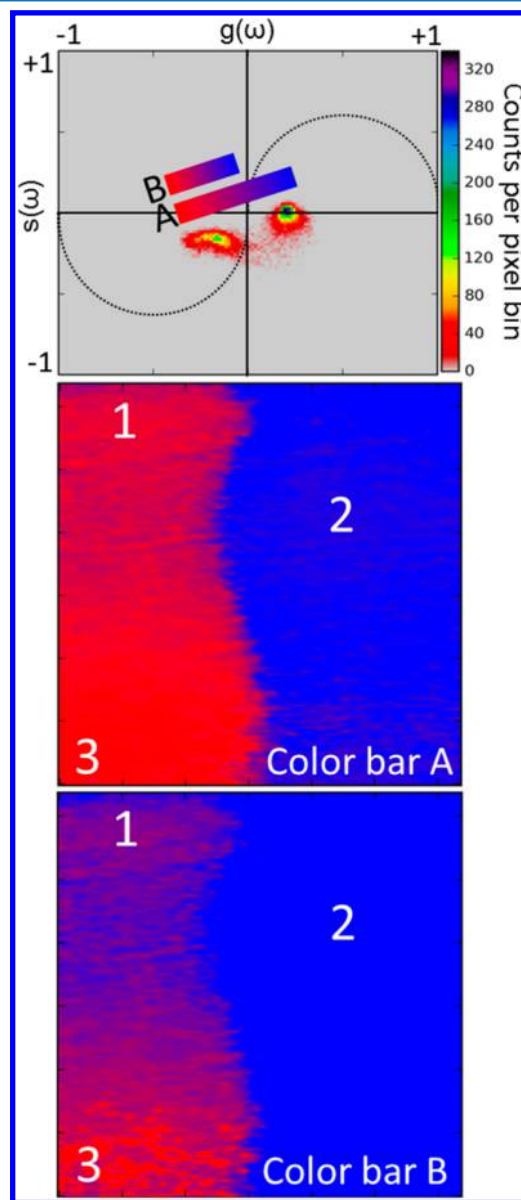


**Figure 3.** Phasor plot of the TAM data set (top).  $g(\omega)$  is the normalized cosinusoidal transform, and  $s(\omega)$  is the normalized sinusoidal transform. The color bar on the right is for the pixel count for each bin on the phasor plot histogram. This phasor plot has 128 bins in each dimension. TAM images recolored based on a phasor analysis with a frequency of 0.5 THz (middle and bottom). Field of view is  $20 \times 20 \mu\text{m}$ . The red-blue color bars, drawn to maximize contrast between clusters, are shown on the phasor plot (top). Color bar A maximizes contrast between regions 2 and 3. Color bar B saturates pixels in region 2, which produces better contrast between regions 1 and 3.

phasor analysis and the associated phasor plot for the chosen TAM data set acquired for the  $\text{CH}_3\text{NH}_3\text{PbI}_3/\text{PCBM}$  polycrystalline thin film as shown in Figure 1.

The extent to which distinct photoexcitation or chemical species populations can be separated is strongly dependent upon the selected phasor frequency; separating TA responses based on differences in their short-lived features requires a high



frequency, whereas separating responses based on their long-lived features requires a low frequency. For the analysis shown in Figure 3, the selected frequency is 0.5 THz. With this frequency, good separation is obtained between the two distinct signals in the phasor plot (Figure 3); we previously attributed these to charge carriers at position 2 and excitons at position 3.

There is also some separation between corresponding pixels for regions 1 and 3, which are contained in the cluster located at the red end of the color bar. Because this cluster of pixels appears to be smeared out toward the blue end of the color bar, it suggests that region 1 is most likely a mixture of photoexcitation species (i.e., a combination of carriers and excitons that give an “intermediate” transient response that is more in the middle of the color bar). Due to the close proximity of pixels from regions 1 and 3 on the phasor plot, the red-blue color bar must be adjusted to maximize contrast between these two areas and the corresponding excited-state character. Saturating the pixels in region 2 allows the dynamic range of the color bar to span the cluster representing pixels in regions 1 and 3, shown in Figure 3. It is interesting to note that there is an uneven pixel distribution on the phasor plot: the pixels that correspond to regions 1 and 3 are concentrated at the red end of color bar rather than having a continuous distribution across the color bar. This suggests that at region 1, where the two photoexcitation species overlap spatially, there is a larger contribution to the TA response from neutral excitons than free charge carriers.

It should be emphasized that phasor analysis excels at finding pixels with similar temporal dynamics, but it provides limited quantitative information: contrast is based on the shape of the TA response but not the amplitude. Given that phasor analysis is a powerful tool for qualitatively exploring the contributing species within a data set, we used it in conjunction with a more quantitative technique. Specifically, we identify regions of interest that have unique temporal responses and then use the average temporal response of those regions as a quantitative internal reference to extract more quantitative information.

## ■ LINEAR DECOMPOSITION

Linear decomposition is a simple approach to reduce the dimensionality of a data set by defining TA response reference curves that are descriptive of the TA signals present in the data set. If possible, the reference curves should be based on experimental data from a separate measurement of the pure species under identical experimental conditions (pump and probe intensities, wavelengths, beam focal spot sizes, etc.). If such a sample is not available, as is the case with photoexcitation species in  $\text{CH}_3\text{NH}_3\text{PbI}_3/\text{PCBM}$  thin films, internal references can be selected from the acquired data set by using phasor analysis or some other data analysis approach to identify the individual contributions from each of the distinct species.

A detailed description about the implementation of linear decomposition is given in the Supporting Information. For the analysis of the TAM data set acquired for the  $\text{CH}_3\text{NH}_3\text{PbI}_3/\text{PCBM}$  thin films, two time-varying reference curves and one dc offset were chosen as our basis set for linear decomposition after exploring the data set with several methods including the phasor plot (Figure 3), *k*-means cluster analysis,<sup>41</sup> and principal component analysis (see Supporting Figures S2–4 and relevant text). We further performed separate calculations of linear decomposition with and without the dc offset component and found that inclusion of the dc offset leads to a significantly

improved fit to the data set. The dc offset term amounts to a spatially varying term that is so long-lived that it is essentially constant in time on this time scale.

The reference curves were averages of responses from regions 2 and 3 based on the results of phasor analysis described in the preceding section. The size of these reference regions was chosen to maximize the signal-to-noise ratio while ensuring that the selected pixels are descriptive of the distinct TA responses, as suggested by the phasor analysis results. Those pixels that were averaged together to create the references are indicated by the boxes in Figure 1, and the reference curves are shown in Figure 2. Accordingly, the results of linear decomposition will generate two distribution maps corresponding to these two input reference curves in addition to a dc offset map that describes differences in signal amplitudes at negative times, which possibly is due to slow geminate recombination<sup>42</sup> or the presence of long-lived trapped carriers.<sup>33,43,44</sup>

These distribution maps can be plotted individually (Figure 4a, b, and c) or overlaid to make an RGB image if all three reference curves are included or just a red-blue image if there are only two standards after excluding the third standard with constant value (Figure 4d). For ease of visualization, each color layer in Figure 4d is normalized so the largest coefficient is 1. Note that a dc offset for each pixel in the image is included in this analysis that describes the residual excited-state populations that do not relax completely before the next pump/probe pulse pair arrives at the sample. Thus, these dc offset values should vary across the entire image, as can be seen in Figure 4c, and represent persistent excited-state populations on the  $\sim 4 \mu\text{s}$  time scales, in agreement with previous work showing long-lived carriers and/or trapped carriers as well as thermal contributions to the TA response.<sup>14,42</sup>

For completeness, we also performed linear decomposition analysis based on the first two principal components obtained with PCA, and the resulting image is shown in Supporting Figure S2 (right). Although the results shown in Figure 4 and Supporting Figure S2 appear similar, we believe that phasor analysis is more appropriate for this work rather than PCA for two reasons. First, phasor analysis identifies pixels with the most distinct TA response curves, whereas PCA finds components that are most common for the entire image. Second, components found with PCA must be orthogonal to one another, but this constraint is not necessarily physical for the actual TA responses of the species, whereas phasor analysis does not impose this constraint.

One important source of error using linear decomposition comes from the quality of the fit. If the data are too noisy (e.g., in areas where the edges of large positive and negative TA signal regions overlap, the resulting superposition leads to nearly zero amplitude) or the reference curves do not accurately describe the data, then the calculated coefficient may be negative. Of course, a negative contribution from one or more of the reference curves is unphysical. To address this, one could force every negative coefficient to zero, but that would imply that the TA response curve perfectly matches the chosen reference curve(s), which is not necessarily the case. Another option is to set the coefficients to zero in every channel, effectively filtering out this portion of data as predominantly composed of noise. To determine the appropriate way to handle negative coefficients, pixels with negative coefficients were plotted (shown in Supporting Information Figure S1). The vast majority of pixels that had negative coefficients were

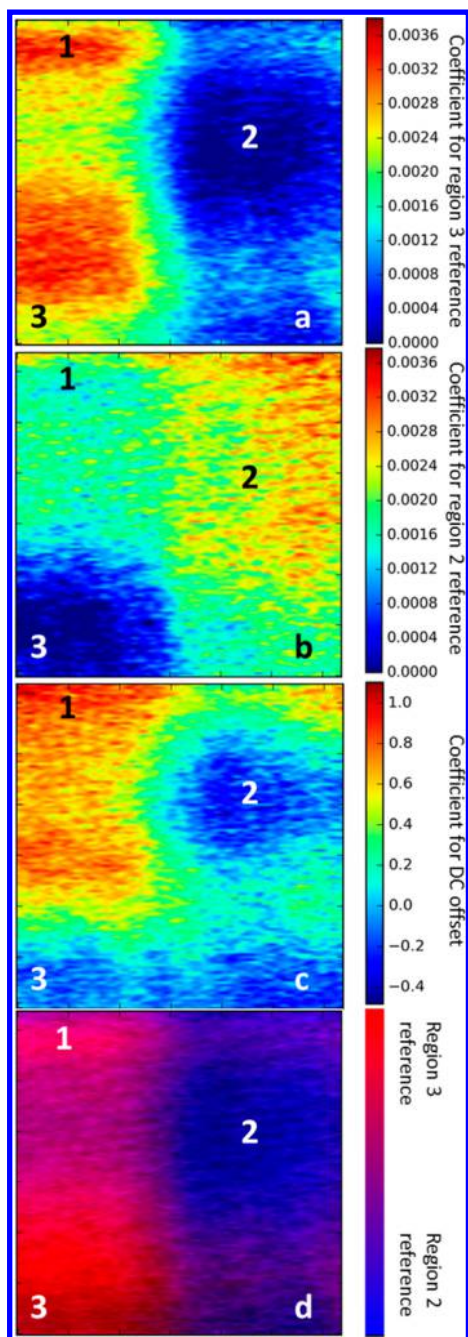


**Figure 4.** Distribution map of the calculated coefficients associated with the region 3 and region 2 references as shown in Figure 2, which were attributed to neutral excitons (a) and free charge carriers (b), respectively. Distribution map of the coefficients associated with a spatially dependent but temporally constant baseline (c). TAM data set in false-color red to blue using the results of linear decomposition (d). The red channel is descriptive of the amplitudes in (a), and the blue channel is descriptive of those amplitudes in (b). Fields of view are  $20 \times 20 \mu\text{m}$ .

located within the regions that were used for calculating reference curves, which suggests that forcing the negative coefficient to zero is appropriate in this case. The second reference curve is unnecessary to describe these regions and, when included, adds unphysical signs to the amplitudes. Because these pixels should match the reference curve and certainly are not among the noisiest in the image, only negative coefficients are set to zero rather than setting all coefficients

associated with those pixels to zero; this eliminates the second reference curve from the equation.

Analysis of the residuals offers a straightforward indication on how well the reference curves and associated coefficients describe the original data. This is achieved by calculating the square root of the sum-squared difference between the original data and the data with reduced dimensionality. Because regions with high signal levels inherently have high noise levels, another way to analyze the residuals is to calculate the residual fraction by dividing by the total amount of signal present, as defined by eq 1:

$$\text{residual fraction} = \frac{\sqrt{\sum (b - Ax)^2}}{\sqrt{\sum b^2}} \quad (1)$$

where  $A$  represents the TA response reference curves at  $N$  time points,  $b$  is the original data (the TA response curves at  $N$  time points that are associated with each of  $M$  pixels in an image), and the solution,  $x$ , contains the coefficients associated with each reference curve for each of  $M$  pixels in the image. Every pixel in the residual image contains the sum of the residual at each time step, which measures the portion of the original TAM data set that is not captured by the reduced dimension data set. Although normalizing by the total signal highlights regions with low TA signal, this normalization does offer a simple way of judging the quality of the linear fit for most spatial regions with a reasonable amount of signal. As can be seen from Figure 5, the residual fraction appears high in areas

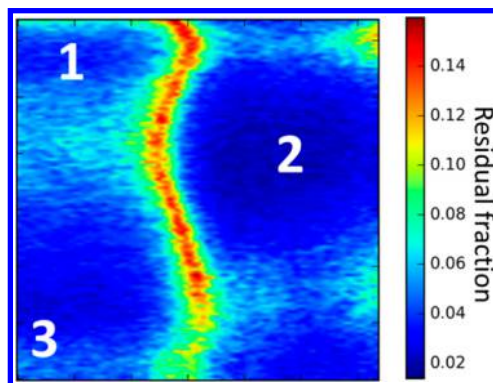


**Figure 5.** Map of the residual fraction, calculated using eq 1. The average residual fraction for the entire image is 0.04. The residual fraction is high only in regions with low signal levels. Field of view is  $20 \times 20 \mu\text{m}$ .

where there is practically no signal, but on average, the residual fraction is fairly low at about 0.04. Note that the residual fractions are similar in region 1 compared to regions 2 and 3; this means that the internal TA response reference curves taken from regions 2 and 3 are able to represent the response in region 1 satisfactorily. If, instead, there were regions with systematically high residual fraction that could not be explained by low signal levels in the original data, then an additional standard or a different standard would be required for accurate dimensionality reduction. For comparison, the absolute residual map is also provided, shown in Supporting Figure S5. The absolute residual map is nearly identical to a map of the total amplitude, shown in Supporting Figure S6. It should be noted that any noise, filtered from the images due to processing the data with linear decomposition, will also inflate the total

residual and residual percentage, despite the fact that noise removal is a benefit of using linear decomposition.

For qualitative analysis shown in Figure 4d, each color channel was normalized to itself in order to map the distributions of each photoexcitation species, but for quantitative analysis, the color scale needs to represent the relative contribution of each reference curve to the total TA response, as will be discussed later. Therefore, we use eq 2 to calculate the relative contribution of each reference curve to the total response. For each pixel, the coefficient for each reference curve is divided by the sum of the coefficients for all reference curves.

$$\text{relative contribution}_{P,R} = \frac{A_{P,R}}{A_{P,1} + A_{P,2}} \quad (2)$$

The notation in eq 2 is the same as that in eq 1;  $P$  is a given pixel, and  $R$  is a given reference (in this case,  $R$  can be either 1 or 2). The relative contribution images are calculated for each reference curve, and then, the channels are overlaid to make a red-blue image, where red represents a TA response derived from the red standard (i.e., region 3) and blue is derived from the blue standard (i.e., region 2).

This new quantitative color scheme is based on the amount that each reference curve contributes to the total TA response, but this omits one crucial piece of quantitative information: the total amplitude of the pixel. To represent the total amplitude that is present in each pixel, a transparency map is overlaid on the color image, which is based on the sum of the amplitudes associated with each species including the dc offset ( $A_{P,3}$ ).

$$\text{total amplitude}_P = A_{P,1} + A_{P,2} + A_{P,3} \quad (3)$$

The notation in eq 3 is identical to that in eq 2. In other words, the color of each pixel is based on the shape of the TA response curve, and the intensity of that color is a representation of the amplitude of the TA response curve. Figure 6 shows the TAM

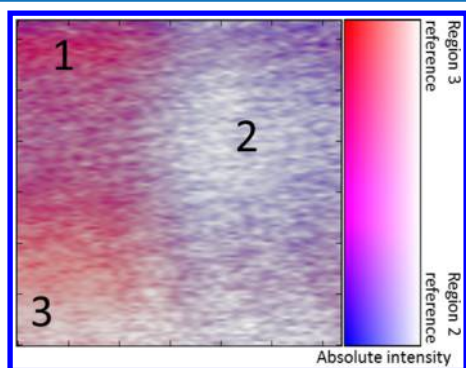


**Figure 6.** Quantitative chemical image calculated using linear decomposition. Color scheme is based on the standards used for linear decomposition (Figure 4). The red-blue color channels are based on the relative portion of the TA response from each standard (eq 2), and the grayscale alpha map is based on the sum of the amplitudes associated with the standards (eq 3). Field of view is  $20 \times 20 \mu\text{m}$ .

data set analyzed with linear decomposition in this more quantitative manner. We found that a representative pixel from region 1 contains approximately 37% blue contribution.

As indicated in Figure 6, although the free charge carriers are characterized by a larger absolute peak amplitude in the TA response curve at early times, these signals represent an overall

smaller portion of the TA response when compared to neutral excitons. On the other hand, the TA response curve associated with neutral excitons is characterized by a smaller peak amplitude at early times but an overall larger contribution of the TA response as a result of this species, at least in the pixels where the species is present (region 1). This is also in agreement with the results of the phasor analysis: pixels with a TA response that results from a mixture of free charge carriers and neutral excitons (such as those in region 1) derive most of their response from the neutral excitons and little from the free charge carriers, although both species are present. Likewise, the presence of neutral excitons masks the existence of the free charge carriers in region 1 where they spatially coexist, as shown in Figures 1 and 2. In other words, because the TA responses associated with neutral excitons and free charge carriers are opposite in sign, the peak amplitudes in regions containing mixtures is artificially low due to the superposition of two signals with different signs obscuring one another.

Importantly, it should be noted that these findings do not give any information regarding actual populations of the photoexcitation species, as that would require knowledge of their absorption cross sections and the branching ratio if the excitons are direct photoexcitations which subsequently undergo rapid dissociation into free charge carriers, as suggested previously.<sup>14</sup> This is beyond the scope of this work. Rather, our results reveal spatial regions where excitons and charge carriers coexist and give an approximate measurement of the amount that each contributes to the observed transient absorption response.

## SUMMARY

We have isolated the spatially dependent contribution of excitons and charge carriers by analyzing measured excited-state relaxation dynamics using a combination of phasor analysis and linear decomposition. It was found that there is a spatially diffuse distribution of pixels that can be described by a relatively low amplitude TA response associated with free charge carriers, and there is a more prominent and spatially localized distribution of pixels having a larger amplitude TA response that is associated with excitonic dynamics. Regions of their coexistence were identified, and through quantitative analysis, the contributions to these areas from each of the photoexcited species were assessed. The approach demonstrated here shows that it is possible to distinguish the spatial distributions of different photoexcited species in spatially heterogeneous systems and should be applicable to the quantitative analysis of other semiconducting materials with coexisting photoexcitations.

An unambiguous understanding about the nature of photoexcitations in thin-film-based photovoltaics and its correlation with the film morphology not only is important from a fundamental perspective but also can serve as a useful guideline for the rational design and fabrication of more efficient devices. Such an understanding is of particular interest for solution-processed hybrid perovskite photovoltaics owing to their remarkable performance and highly heterogeneous morphologies, which depend strongly on device fabrication and processing conditions. As shown by our recent steady-state two-photon fluorescence imaging measurement, variation of thermal annealing time can profoundly affect the emission intensity, its spatial distribution, and orientation of the associated electronic dipole moments.<sup>45</sup> On the basis of this observation, we plan to further examine perovskite samples



prepared under differing preparation protocols to determine the extent of the heterogeneity of photoexcitation products observed here, as well as other photovoltaic materials, including organic photovoltaics.

We would like to emphasize that our findings are based on femtosecond TAM measurements on planar thin films of  $\text{CH}_3\text{NH}_3\text{PbI}_3$  coated with PCBM layers, whose preparation involved ambient air exposure followed by 120 min thermal annealing at 100 °C under a  $\text{N}_2$  atmosphere. The thin films prepared by this procedure have been shown to form large single-crystal grains with size exceeding 2  $\mu\text{m}$ .<sup>46</sup> Our findings are in line with a recent report by Grancini et al.;<sup>31</sup> these authors showed that both free carriers and excitons are possible depending on sample fabrication procedures and morphology. Specifically, the authors observed a sharp excitonic feature in the linear absorption spectrum and femtosecond transient absorption spectra acquired at room temperature for a  $\text{CH}_3\text{NH}_3\text{PbBr}_3$  thin film with average crystal dimensions of approximately  $\sim 1 \mu\text{m}$ . Given the ongoing debate regarding the nature of photoexcitations in this material, which arises at least partially from the diverse values of the reported exciton binding energies for three-dimensional halide perovskite materials ranging from several tens of meV<sup>14,16,18–23</sup> to as small as a few meV,<sup>24,47</sup> further experiments on thin film samples with well-defined morphologies will be needed to unambiguously settle this question. Moreover, although the hot-carrier cooling effect reported very recently<sup>48</sup> may alter the transient absorption signal sign probed at both higher and lower energy sides of the band-edge, its potential contribution to our experimental results remains to be addressed in future studies. This is because the hot-carrier cooling rates depend strongly on photogenerated carrier density, level of defects and impurities, and spatial confinement of the samples under study,<sup>49</sup> which are significantly different in our experiment and that of Price et al. In view of the high spatial heterogeneity associated with the solution-processed perovskite films and the fact that significant morphological changes can be introduced by slight alternation of sample preparation and processing, we believe that it is important to take into account the thin film morphologies when comparing optical spectroscopic and microscopic data reported by different laboratories.

## METHODS

Details about the sample preparation, femtosecond TAM apparatus, and data acquisition were described previously.<sup>25</sup> Briefly, two-color femtosecond transient absorption microscopic images were collected with pump and probe pulses centered at 500 and 800 nm, respectively. The light source was a 250 kHz femtosecond Ti:sapphire amplifier laser (Coherent RegA 9050) pumping an optical parametric amplifier. After passing through independent prism compressors, the collinear pump and probe beams were directed into a modified commercial inverted white light microscope (Eclipse TE 300, Nikon). A 40 $\times$  objective with a 0.72 NA (Nikon) was used to focus the spatially overlapped beams onto a perovskite sample through a coverslip. Transmitted light was collected using a 2 $\times$ , 0.06 NA objective and sent through appropriate pump-rejection spectral filters before being focused onto a balanced photodiode that is read out with a lock-in amplifier (SR 810 DSP, Stanford Research Systems). Data acquisition involves scanning the sample stage within the focal plane of the pump and probe beams at each of 68 delay times, resulting in a data set consisting of a stack of 68, 128  $\times$  128 pixel data arrays of a 20

$\mu\text{m} \times 20 \mu\text{m}$  region of interest. All data processing programs were written in Python.

The temporal resolution is estimated to be 200–300 fs, and the spatial resolution was estimated to be about 330 nm. The former is limited by the pulse widths of our pump and probe beams, whereas the latter is dictated by the wavelengths used (500 and 800 nm) and numerical aperture of the objective (0.72 NA). The lowest possible power level that still produced transient absorption signals with a sufficient signal-to-noise ratio was 13.1  $\mu\text{W}$  for the pump and 7.0  $\mu\text{W}$  for the probe with corresponding fluences of  $\sim 10$  and  $\sim 2.1 \text{ mJ}/\text{cm}^2$ , respectively, assuming diffraction-limited spot sizes. The values decrease to  $\sim 68.0 \mu\text{J}/\text{cm}^2$  for the pump and 5.1  $\mu\text{J}/\text{cm}^2$  for the probe based on the spot sizes determined experimentally. Although the power used for our measurement is relatively high, it allows one to measure nonlinear relaxation dynamics such as Auger and exciton–exciton annihilation processes that enable us to map the spatial localization of carriers and excitons in the sample.

The polycrystalline  $\text{CH}_3\text{NH}_3\text{PbI}_3$  thin film was prepared on a glass coverslip following a procedure described previously.<sup>46</sup> PCBM was dissolved in chlorobenzene to prepare a solution with a concentration of 20 mg/mL, and this PCBM solution was spin-coated at 1500 rpm for 30 s on top of the glass/ $\text{CH}_3\text{NH}_3\text{PbI}_3$  films. A 100  $\mu\text{m}$  thick microscope glass coverslip was used to cover the samples, which was then encapsulated with UV epoxy in an  $\text{N}_2$ -filled glovebox.

## ASSOCIATED CONTENT

### Supporting Information

The Supporting Information is available free of charge on the ACS Publications website at DOI: 10.1021/acsphotonics.5b00638.

A validation of the analysis method separating distinct species; additional details about false-coloring the data set; details about implementation of linear decomposition; a justification for using only two time-varying reference curves to represent the data set; further analysis of the residuals (PDF)

## AUTHOR INFORMATION

### Corresponding Author

\*E-mail (Y.-Z. Ma): [may1@ornl.gov](mailto:may1@ornl.gov).

### Notes

The authors declare no competing financial interest.

## ACKNOWLEDGMENTS

M.J.S., B.D., and Y.-Z.M. were supported by the U.S. Department of Energy, Office of Science, Basic Energy Sciences, Chemical Sciences, Geosciences, and Biosciences Division. Perovskite sample preparation by B.Y. and K.X. was performed at the Center for Nanophase Materials Sciences (CNMS), which is a DOE Office of Science User Facility. M.J.S. thanks Michael J. Simpson, Jesse W. Wilson, and Francisco E. Robles for sharing their data analysis expertise through helpful discussions and trouble-shooting Python scripts.

## REFERENCES

- (1) Fu, D.; Matthews, T. E.; Ye, T.; Piletic, I. R.; Warren, W. S. Label-Free in Vivo Optical Imaging of Microvasculature and Oxygenation Level. *J. Biomed. Opt.* **2008**, *13*, 040503.

- (2) Min, W.; Lu, S.; Chong, S.; Roy, R.; Holtom, G. R.; Xie, X. S. Imaging Chromophores with Undetectable Fluorescence by Stimulated Emission Microscopy. *Nature* **2009**, *461*, 1105–1109.
- (3) Hartland, G. V. Ultrafast Studies of Single Semiconductor and Metal Nanostructures through Transient Absorption Microscopy. *Chem. Sci.* **2010**, *1*, 303–309.
- (4) Huang, L.; Hartland, G. V.; Chu, L.-Q.; Luxmi, Feenstra, R. M.; Lian, C.; Tahy, K.; Xing, H. Ultrafast Transient Absorption Microscopy Studies of Carrier Dynamics in Epitaxial Graphene. *Nano Lett.* **2010**, *10*, 1308–1313.
- (5) Polli, D.; Grancini, G.; Clark, J.; Celebrano, M.; Virgili, T.; Cerullo, G.; Lanzani, G. Nanoscale Imaging of the Interface Dynamics in Polymer Blends by Femtosecond Pump-Probe Confocal Microscopy. *Adv. Mater.* **2010**, *22*, 3048–3051.
- (6) Matthews, T. E.; Piletic, I. R.; Selim, M. A.; Simpson, M. J.; Warren, W. S. Pump-Probe Imaging Differentiates Melanoma from Melanocytic Nevi. *Sci. Transl. Med.* **2011**, *3*, 71ra15.
- (7) Wang, P.; Slipchenko, M. N.; Mitchell, J.; Yang, C.; Potma, E. O.; Xu, X.; Cheng, J.-X. Far-Field Imaging of Non-Fluorescent Species with Subdiffraction Resolution. *Nat. Photonics* **2013**, *7*, 449–453.
- (8) Grumstrup, E. M.; Gabriel, M. M.; Pinion, C. W.; Parker, J. K.; Cahoon, J. F.; Papanikolas, J. M. Reversible Strain-Induced Electron-Hole Recombination in Silicon Nanowires Observed with Femtosecond Pump-Probe Microscopy. *Nano Lett.* **2014**, *14*, 6287–6292.
- (9) Simpson, M. J.; Wilson, J. W.; Phipps, M. A.; Robles, F. E.; Selim, M. A.; Warren, W. S. Nonlinear Microscopy of Eumelanin and Pheomelanin with Subcellular Resolution. *J. Invest. Dermatol.* **2013**, *133*, 1822–1826.
- (10) Robles, F. E.; Wilson, J. W.; Fischer, M. C.; Warren, W. S. Phasor Analysis for Nonlinear Pump-Probe Microscopy. *Opt. Express* **2012**, *20*, 17082.
- (11) Simpson, M. J.; Glass, K. E.; Wilson, J. W.; Wilby, P. R.; Simon, J. D.; Warren, W. S. Pump-Probe Microscopic Imaging of Jurassic-Aged Eumelanin. *J. Phys. Chem. Lett.* **2013**, *4*, 1924–1927.
- (12) Villafañá, T. E.; Brown, W. P.; Delaney, J. K.; Palmer, M.; Warren, W. S.; Fischer, M. C. Femtosecond Pump-Probe Microscopy Generates Virtual Cross-Sections in Historic Artwork. *Proc. Natl. Acad. Sci. U. S. A.* **2014**, *111*, 1708–1713.
- (13) Zhou, H.; Chen, Q.; Li, G.; Luo, S.; Song, T.-b.; Duan, H.-S.; Hong, Z.; You, J.; Liu, Y.; Yang, Y. Interface Engineering of Highly Efficient Perovskite Solar Cells. *Science* **2014**, *345*, 542–546.
- (14) Savenije, T. J.; Ponseca, C. S.; Kunnenman, L.; Abdellah, M.; Zheng, K. B.; Tian, Y. X.; Zhu, Q. S.; Canton, S. E.; Scheblykin, I. G.; Pullerits, T.; Yartsev, A.; Sundström, V. Thermally Activated Exciton Dissociation and Recombination Control the Carrier Dynamics in Organometal Halide Perovskite. *J. Phys. Chem. Lett.* **2014**, *5*, 2189–2194.
- (15) Hsu, H.-Y.; Wang, C.-Y.; Fathi, A.; Shiu, J.-W.; Chung, C.-C.; Shen, P.-S.; Guo, T.-F.; Chen, P.; Lee, Y.-P.; Diau, E. W. G. Femtosecond Excitonic Relaxation Dynamics of Perovskite on Mesoporous Films of Al<sub>2</sub>O<sub>3</sub> and NiO Nanoparticles. *Angew. Chem., Int. Ed.* **2014**, *53*, 9339–9342.
- (16) Wu, K.; Bera, A.; Ma, C.; Du, Y.; Yang, Y.; Li, L.; Wu, T. Temperature-Dependent Excitonic Photoluminescence of Hybrid Organometal Halide Perovskite Films. *Phys. Chem. Chem. Phys.* **2014**, *16*, 22476–22481.
- (17) Deschler, F.; Price, M.; Pathak, S.; Klintberg, L. E.; Jarausch, D.-D.; Högler, R.; Hüttner, S.; Leijtens, T.; Stranks, S. D.; Snaith, H. J.; Atatüre, M.; Phillips, R. T.; Friend, R. H. High Photoluminescence Efficiency and Optically Pumped Lasing in Solution-Processes Mixed Halide Perovskite Semiconductors. *J. Phys. Chem. Lett.* **2014**, *5*, 1421–1426.
- (18) D'Innocenzo, V.; Grancini, G.; Alcocer, M. J. P.; Kandada, A. R. S.; Stranks, S. D.; Lee, M. M.; Lanzani, G.; Snaith, H. J.; Petrozza, A. Excitons Versus Free Charges in Organo-Lead Tri-Halide Perovskites. *Nat. Commun.* **2014**, *5*, 3586.
- (19) Ishihara, T. Optical Properties of PbI<sub>2</sub>-Based Perovskite Structures. *J. Lumin.* **1994**, *60&61*, 269–274.
- (20) Sun, S. Y.; Salim, T.; Mathews, N.; Duchamp, M.; Boothroyd, C.; Xing, G. C.; Sum, T. C.; Lam, Y. M. The Origin of High Efficiency in Low-Temperature Solution-Processable Bilayer Organometal Halide Hybrid Solar Cells. *Energy Environ. Sci.* **2014**, *7*, 399–407.
- (21) Hirasawa, M.; Ishihara, T.; Goto, T.; Uchida, K.; Miura, N. Magnetoabsorption of the Lowest Exciton in Perovskite-Type Compound (CH<sub>3</sub>NH<sub>3</sub>)PbI<sub>3</sub>. *Phys. B* **1994**, *201*, 427–430.
- (22) Koutselas, I. B.; Ducasse, L.; Papavassiliou, G. C. Electronic Properties of Three- and Low-Dimensional Semiconducting Materials with Pb Halide and Sn Halide Units. *J. Phys.: Condens. Matter* **1996**, *8*, 1217–1227.
- (23) Tanaka, K.; Takahashi, T.; Ban, T.; Kondo, T.; Uchida, K.; Miura, N. Comparative Study on the Excitons in Lead-Halide-Based Perovskite-type Crystals CH<sub>3</sub>NH<sub>3</sub>PbBr<sub>3</sub>, CH<sub>3</sub>NH<sub>3</sub>PbI<sub>3</sub>. *Solid State Commun.* **2003**, *127*, 619–623.
- (24) Lin, Q.; Armin, A.; Nagiri, R. C. R.; Burn, P. L.; Meredith, P. Electro-Optics of Perovskite Solar Cells. *Nat. Photonics* **2015**, *9*, 106–112.
- (25) Simpson, M. J.; Doughty, B.; Yang, B.; Xiao, K.; Ma, Y.-Z. Spatial Localization of Excitons and Charge Carriers in Hybrid Perovskite Thin Films. *J. Phys. Chem. Lett.* **2015**, *6*, 3041–3047.
- (26) van Amerongen, H.; Valkunas, L.; van Grondelle, R. *Photosynthetic Excitons*; World Scientific: London, 2000.
- (27) Ghanassi, M.; Schanne-Klein, M. C.; Hache, F.; Ekimov, A. I.; Ricard, D.; Flytzanis, C. Time-Resolved Measurements of Carrier Recombination in Experimental Semiconductor-Doped Glasses: Confirmation of the Role of Auger Recombination. *Appl. Phys. Lett.* **1993**, *62*, 78–80.
- (28) Klimov, V. I.; Mikhailovsky, A. A.; McBranch, D. W.; Leatherdale, C. A.; Bawendi, M. G. Quantization of Multiparticle Auger Rates in Semiconductor Quantum Dots. *Science* **2000**, *287*, 1011–1013.
- (29) Htoon, H.; Hollingsworth, J. A.; Dickerson, R.; Klimov, V. I. Effect of Zero- to One-Dimensional Transformation on Multiparticle Auger Recombination in Semiconductor Quantum Rods. *Phys. Rev. Lett.* **2003**, *91*, 227401.
- (30) Ma, Y.-Z.; Valkunas, L.; Bachilo, S. M.; Fleming, G. R. Exciton Binding Energy in Semiconducting Single-Walled Carbon Nanotubes. *J. Phys. Chem. B* **2005**, *109*, 15671–15674.
- (31) Grancini, G.; Kandada, A. R. S.; Frost, J. M.; Barker, A. J.; De Bastiani, D.; Gandini, M.; Marras, S.; Lanzani, G.; Walsh, A.; Petrozza, A. Role of Microstructure in the Electron–Hole Interaction of Hybrid Lead Halide Perovskites. *Nat. Photonics* **2015**, *9*, 695–701.
- (32) Wang, H.; Whittaker-Brooks, L.; Fleming, G. R. Exciton and Free Charge Dynamics of Methylammonium Lead Iodide Perovskites Are Different in the Tetragonal and Orthorhombic Phases. *J. Phys. Chem. C* **2015**, *119*, 19590–19595.
- (33) Stranks, S. D.; Burlakov, V. M.; Leijtens, T.; Ball, J. M.; Goriely, A.; Snaith, H. J. Recombination Kinetics in Organic-Inorganic Perovskites: Excitons, Free Charges, and Subgap States. *Phys. Rev. Appl.* **2014**, *2*, 034007.
- (34) Wetzelaer, G. A. H.; Scheepers, M.; Sempere, A. M.; Momblona, C.; Avila, J.; Bolink, H. J. Trap-Assisted Non-Radiative Recombination in Organic–Inorganic Perovskite Solar Cells. *Adv. Mater.* **2015**, *27*, 1837–1841.
- (35) deQuilettes, D. W.; Vorpahl, S. M.; Stranks, S. D.; Nagaoka, H.; Eperon, G. E.; Ziffer, M. E.; Snaith, H. J.; Ginger, D. S. Impact of Microstructure on Local Carrier Lifetime in Perovskite Solar Cells. *Science* **2015**, *348*, 683–686.
- (36) Bischak, C. G.; Sanehira, E. M.; Precht, J. T.; Luther, J. M.; Ginsberg, N. S. Heterogeneous Charge Carrier Dynamics in Organic–Inorganic Hybrid Materials: Nanoscale Lateral and Depth-Dependent Variation of Recombination Rates in Methylammonium Lead Halide Perovskite Thin Films. *Nano Lett.* **2015**, *15*, 4799–4807.
- (37) Vrućinić, M.; Matthiesen, C.; Sadhanala, A.; Divitini, G.; Cacovich, S.; Dutton, S. E.; Ducati, C.; Atatüre, M.; Snaith, H.; Friend, R. H.; Sirringhaus, H.; Deschler, F. Local Versus Long-Range Diffusion Effects of Photoexcited States on Radiative Recombination in



Organic–Inorganic Lead Halide Perovskites. *Adv. Sci.* **2015**, *2*, 1500136.

(38) Guo, Z.; Manser, J. S.; Wan, Y.; Kamat, P. V.; Huang, L. Spatial and Temporal Imaging of Long-Range Charge Transport in Perovskite Thin Films by Ultrafast Microscopy. *Nat. Commun.* **2015**, *6*, 7471.

(39) Sheng, C. X.; Zhang, C.; Zhai, Y.; Mielczarek, K.; Wang, W.; Ma, W.; Zakhidov, A.; Vardeny, Z. V. Exciton Versus Free Carrier Photogeneration in Organometal Trihalide Perovskites Probed by Broadband Ultrafast Polarization Memory Dynamics. *Phys. Rev. Lett.* **2015**, *114*, 116601.

(40) Digman, M. A.; Caiolfa, V. R.; Zamaï, M.; Gratton, E. The Phasor Approach to Fluorescence Lifetime Imaging Analysis. *Biophys. J.* **2008**, *94*, L14–L16.

(41) Strelcov, E.; Belianinov, A.; Hsieh, Y.-H.; Jesse, S.; Baddorf, A. P.; Chu, Y.-H.; Kalinin, S. V. Deep Data Analysis of Conductive Phenomena on Complex Oxide Interfaces: Physics from Data Mining. *ACS Nano* **2014**, *8*, 6449–6457.

(42) Ponseca, C. S.; Savenije, T. J.; Abdellah, M.; Zheng, K. B.; Yartsev, A.; Pascher, T.; Harlang, T.; Chabera, P.; Pullerits, T.; Stepanov, A.; Wolf, J.-P.; Sundström, V. Organometal Halide Perovskite Solar Cell Materials Rationalized: Ultrafast Charge Generation, High and Microsecond-Long Balanced Mobilities, and Slow Recombination. *J. Am. Chem. Soc.* **2014**, *136*, 5189–5192.

(43) Leijtens, T.; Stranks, S. D.; Eperon, G. E.; Lindblad, R.; Johansson, E. M. J.; McPherson, I. J.; Rensmo, H.; Ball, J. M.; Lee, M. M.; Snaith, H. J. Electronic Properties of Meso-Superstructured and Planar Organometal Halide Perovskite Films: Charge Trapping, Photodoping, and Carrier Mobility. *ACS Nano* **2014**, *8*, 7147–7155.

(44) Oga, H.; Saeki, A.; Ogomi, Y.; Hayase, S.; Seki, S. Improved Understanding of the Electronic and Energetic Landscapes of Perovskite Solar Cells: High Local Charge Carrier Mobility, Reduced Recombination, and Extremely Shallow Traps. *J. Am. Chem. Soc.* **2014**, *136*, 13818–13825.

(45) Watson, B. R.; Yang, B.; Xiao, K.; Ma, Y.-Z.; Doughty, B.; Calhoun, T. R. Elucidation of Perovskite Film Micro-Orientations Using Two-Photon Total Internal Reflectance Fluorescence Microscopy. *J. Phys. Chem. Lett.* **2015**, *6*, 3283–3288.

(46) Yang, B.; Dyck, O.; Poplawsky, J.; Keum, J.; Poretzky, A.; Das, S.; Ivanov, I.; Rouleau, C.; Duscher, G.; Geohegan, D.; Xiao, K. Perovskite Solar Cells with near 100% Internal Quantum Efficiency Based on Large Single Crystalline Grains and Vertical Bulk Heterojunctions. *J. Am. Chem. Soc.* **2015**, *137*, 9210–9213.

(47) Miyata, A.; Mitioglu, A.; Plochocka, P.; Portugall, O.; Wang, J. T.-W.; Stranks, S. D.; Snaith, H. J.; Nicholas, R. J. Direct Measurement of the Exciton Binding Energy and Effective Masses for Charge Carriers in Organic–Inorganic Tri-Halide Perovskites. *Nat. Phys.* **2015**, *11*, 582–587.

(48) Price, M. B.; Butkus, J.; Jellicoe, T. C.; Sadhanala, A.; Briane, A.; Halpert, J. E.; Broch, K.; Hodgkiss, J. M.; Friend, R. H.; Deschler, F. Hot-Carrier Cooling and Photoinduced Refractive Index Changes in Organic–Inorganic Lead Halide Perovskites. *Nat. Commun.* **2015**, *6*, 8420.

(49) Nozik, A. J. Spectroscopy and Hot Electron Relaxation Dynamics in Semiconductor Quantum Wells and Quantum Dots. *Annu. Rev. Phys. Chem.* **2001**, *52*, 193–231.